ARTICLE TYPE

Cite this: DOI: 00.0000/xxxxxxxxxx

Transitioning the transition metal dichalcogenide TcS_2, making the 4d behave like a 3d

Dean Sayre,[a,b], Emily Siska,[a,b] G. Alexander Smith,[a,c] Nicholas Chang,[c] Changyong Park,[d] Frederic Poineau,[c] Craig Schwartz,[a] Keith V. Lawler,[a,*] Ashkan Salamat,[a,b,*]

Received Date
Accepted Date

DOI: 00.0000/xxxxxxxxxx

TcS_2 undergoes an isostructural charge transfer insulator to metal transition at 28 GPa. Laser annealing reveals a kinetically hindered high pressure arsenopyrite phase that is recoverable to ambient. The new phase is similar to Mn rather than Re and involves the formation of S–S and Tc–Tc bonds.

There are two broad classes of structural motifs found within the ambient phases of the transition metal dichalcogenides (TMDCs; MX_2 where X = S, Se, or Te), extended 3-D lattices typically of the pyrite or marcasite type and layered 2-D lattices.[1] For instance, all of group 8 form extended 3d lattices; whereas the heavier 4d and 5d elements of the other groups tend to form layered TMDCs.[1] The unique electronic properties of layered TMDCs, often tunable based on thickness from the bulk to monolayer form, has placed them at the forefront of the recent explosion of research into 2-D materials, leading to their use in catalytic, optoelectronic and photonic applications as well as interest in their topological and superconducting phases.[2–5] Pressure and strain engineering have been demonstrated as ways to manipulate the electronic properties of TMDCs, including driving these typically semiconducting materials into a metallic or superconducting state.[3,5,6]

Within group 7, all of the TMDCs of Mn naturally adopt a pyrite structure at ambient conditions whereas the TMDCs of Re and Tc form layered structures.[7,8] The chalcogens dimerize to form molecular anions in the pyrite Mn TMDC structures, with the resulting high-spin d^5 Mn^{2+} providing interesting behavior in high pressure conditions.[8–10] When the pyrite phase of MnS_2 is compressed it can undergo a negative charge transfer insulator-to-metal transition driven by Mn d electron donation into vacant $(S_2)^{2-}$ antibonding σ^* orbitals which results in a colossal $10^8\,\Omega$ drop in resistance.[11] When compressed beyond metallization or laser heated at sufficient pressure, MnS_2 transforms into its high-pressure, insulating arsenoypyrite phase with a massive (up to 22%) volume drop driven by a high-to-low spin transformation of the Mn d states.[10–12]

The layered structures of ReS_2 and $ReSe_2$ are of the triclinic distorted $CdCl_2$-type structure with Peierls distortions within the monolayers.[7] Both ReS_2 and $ReSe_2$ undergo an isostructural phase transition ~10 GPa, and by ~35 GPa the weakly van der Waals coupled layers metallize as a result of layer-sliding and contraction along planes.[13–17] Other high pressure phases of the Re TMDCs have been predicted, but not clearly demonstrated experimentally.[16,18] Due its radioactivity, Re is often used as a stand-in for Tc chemistry, but instead of following periodic trends TcS_2 adopts a triclinic distorted $Cd(OH)_2$-type structure with chains of bridged Tc atoms.[7,19] Unlike the Mn and Re TMDCs, little is known about the high pressure-high temperature behavior of the Tc TMDCs. Here, we report a joint experimental and theoretical investigation into the high pressure metallization of TcS_2 as well as a new high pressure phase that adopts an extended structure and opens the floor to reinterpretations of the high-pressure phases of other layered TMDCs.

X-ray absorption near-edge spectroscopy (XANES) measurements were performed radially on TcS_2 samples loaded into diamond anvil cells (DAC) using a x-ray transparent Be gasket. Alumina was used as the pressure-transmitting medium (PTM) over two distinct pressure regions ~13–32 and 25–46 GPa to probe for the onset of metallization. Further experimental and simulations details are in the ESI. Fig. 1 shows that the peak at 21,130 eV broadens and increases in energy with respect to pressure, indicative of a shortening of Tc nearest neighbor distances with pressure. The strongest absorption peak near 21,075 eV continuously

---

[a] *Nevada Extreme Conditions Laboratory, University of Nevada, Las Vegas, Las Vegas, Nevada 89154, USA*
[b] *Department of Physics Astronomy, University of Nevada, Las Vegas, Las Vegas, Nevada 89154, USA*
[c] *Department of Chemistry Biochemistry, University of Nevada, Las Vegas, Las Vegas, Nevada 89154, USA*
[d] *HPCAT, X-ray Science Division, Argonne National Laboratory, Illinois 60439, USA*
[*] *E-mail: keith.lawler@unlv.edu, ashkan.salamat@unlv.edu*

† Electronic Supplementary Information (ESI) available: [details of any supplementary information available should be included here]. See DOI: 00.0000/00000000.

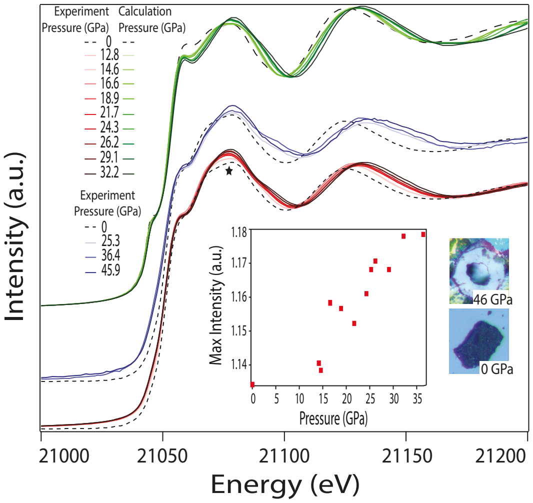

Fig. 1 Experimental XANES spectra from two separate compressions at room temperature (blue and red) and corresponding theoretical curves (green), showing significant matching of the major spectral features. **(Inset)** The maximum peak intensity up to 36 GPa and photos of samples at 0 and 46 GPa.

increases in intensity with pressure. The inset of Fig. 1 shows the roughly monotonically increasing maximum intensity of the first peak as a function of pressure for the first run. The transitions being more localized spatially as pressure increases is believed to drive this increase in transition strength. The onset energy at approximately 21,040 eV shows a continual red-shift with pressure, a behavior consistent with an evolution from the initial phase into a new phase. However, this shift of the onset energy is not significant enough to indicate a change in formal oxidation state away from Tc^{4+} and atomic S^{2-} anions. All of the key features of the experiment are captured in FDMNES[20] simulations (Fig. 1, green) including the 21,130 eV peak blue shifting with pressure, the strongest absorption peak increasing in intensity with pressure and the initial onset energy red-shifting with pressure. The density functional theory (DFT) cluster calculations for the Fermi energy in FDMNES indicate TcS_2 should be metallic by 46 GPa. The sample is also optically observed to develop a metallic-like lustre with compression (Fig. 1 inset), indicative of a transition into a metallic state. Taken together this behavior is consistent with metallization by the highest pressures measured.

This electronic transformation is accompanied by a preservation of crystallographic features up to 33 GPa according to synchrotron angle dispersive X-ray diffraction (XRD) measurements (see ESI) performed axially along with the XANES. By 28 GPa, Raman spectroscopy shows features that are broadened due to the shortening of phonon lifetimes as Raman features saturate (Fig. 3 bottom). Above 36 GPa there is a loss of the characteristic Bragg features of the $P\bar{1}$ crystalline system, with the remaining distinct features in the spectra coming from the alumina PTM. At those pressures the Raman spectrum also exhibits a loss of features. Thus, this pressure induced amorphization drives the system into a glassy-like metallic state.

More sophisticated simulations of the compression of $P\bar{1}$ TcS_2 on 2 GPa intervals between 0–50 GPa using the SCAN+rVV10[21] functional with VASP 5.4.4 confirm the system metallizes by 46 GPa. The ambient phase is a charge transfer insulator with an indirect 1.06 eV band gap, a valence band maximum (VBM) at Z: $\vec{k} = (0,\ 0,\ \frac{1}{2})$, and a conduction band minimum (CBM) at a point in the Brillouin zone near V: $\vec{k} \sim (\frac{1}{2},\ \frac{1}{2},\ 0)$ (Fig. 2a). The band gap closes monotonically with compression, and the CBM and VBM remain at the same points in the Brillouin zone. When the system does metallize at 46 GPa, the VBM shifts to Y: $\vec{k} = (0,\ \frac{1}{2},\ 0)$, and the VBM at that point is comprised predominantly of S p states. The metallization, like the low pressure band gap, is indirect making the system semi-metallic. In addition, the CBM and VBM of the metallic state represent Tc d states and S p states respectively, defining the transition as a charge transfer insulator to metal transition. Bader charge analysis[22] shows the average Tc charge decreasing from 0.964e at 0 GPa to 0.828e at 50 GPa while the average S charge increases from -0.482e at 0 GPa to -0.414e at 50 GPa which is consistent with ligand-to-metal charge transfer and thus a charge transfer insulator to metal transition.

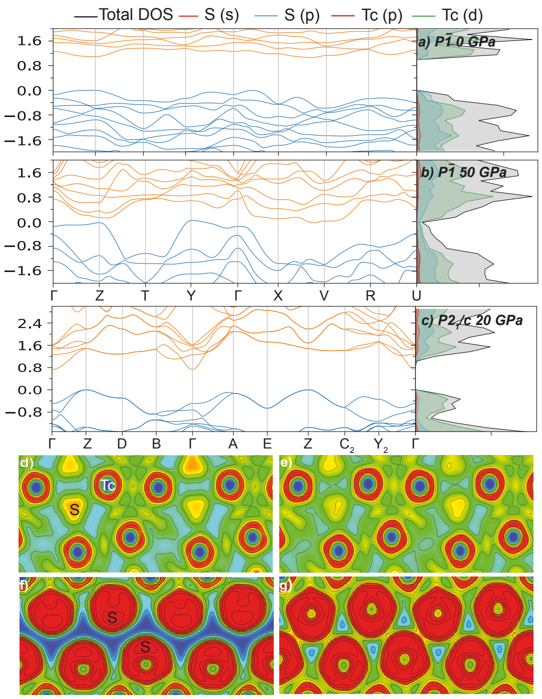

Fig. 2 Band structure and atom and angular momentum decomposed density of states for $P\bar{1}$ TcS_2 at (**a**) 0 and (**b**) 50 GPa, **(c)** as well as 20 GPa $P2_1/c$ TcS_2. ELF at 60% of the maximum saturation value for intralyer (**d-e)** and interlayer (**f-g)** interactions at 0 (left) and 50 (right) GPa. The concentric colors blue, green, and yellow/red correspond to an empty void of electrons, a uniform electron gas, and a complete localization of electrons, respectively.

The electron localization functions (ELF) displayed in Fig. 2d-g provide a real-space visual interpretation of the metallization mechanism described by the pressure evolution of the band structure of $P\bar{1}$ TcS_2. At 0 GPa, the S atoms are polar covalent within their respective 2-D lattices as evidenced by the aspherical triangular distortions of the S charge densities towards their nearest neighbor Tc atoms (Fig. 2d). As anticipated by the weakly van der Waals bound model for layered TMDCs, there is a void of interlayer charge density at 0 GPa (Fig. 2f). Compression to 50 GPa does not alter the intralayer bonding scheme of TcS_2 significantly (Fig. 2e) except for the formation of very weak S–S interactions. However, the interlayer picture shows a significantly stronger S–S interaction forming between the compressed layers at 50 GPa (Fig 2g). The shape of the interlayer S–S interactions at 50 GPa is reminiscent of a persulfide $(S_2)^{2-}$ unit, in particular the accumulation of charge density along the line of centers, yet the simulations and XANES still dictate these are atomic anions.

Further structural analysis with DFT reveals a dramatic $\sim$12% change in the c/a ratio between the $P\bar{1}$ TcS_2 structures at 0 and 50 GPa whereas the b/a, γ/α, and β/α ratios all differ below a few percent. The collapse in c/a results in a 33% reduction of the interlayer sulfur distances which is driving the formation of the interlayer S–S interactions (Fig 2g). Meanwhile, the Tc–S intralayer distances are relatively preserved, differing by only 3–7% from 0 to 50 GPa, indicating little change in the intralayer bonding as evidenced by the ELFs in Fig. 2d,e. This is in line with pressure induced metallization in other 2-D TMDCs where the interlayer van der Waals force competes with a pressure-driven force in the stacking direction of the TMDC layers.[6,15–17,23] Specifically, the metallization being driven by increased S–S interactions in between the layers is very similar to what has been observed for ReS_2 and MoS_2.[17,23]

Pressure induced amorphization of a material can often indicate a kinetically hindered competing phase further driven by non-hydrostaticity.[11] Exploring alternate compression pathways can lead to different structural and electronic responses in materials which can overcome kinetic hindrance, so TcS_2 was compressed and laser heated (1070 nm) at 30 GPa in a quasi-hydrostatic Ar PTM (with an NaCl thermal insulator) to probe for a new high pressure phase. Room temperature compression in the Ar PTM produced samples with poorly-defined peaks in contrast to the mostly featureless spectrum observed previously in the highly non-hydrostatic alumina PTM (Fig. 3 top). Laser heating was first attempted with a CO_2 laser on compressed $P\bar{1}$ TcS_2, but it was not found to couple well. Heating was then switched to a Nd:YAG laser which did couple well, further indications that compressed $P\bar{1}$ TcS_2 is a small gap or metallic system. During laser heating the sample was probed with Raman spectroscopy, and after a few minutes the sample had transformed into a uniform new phase with a distinct set of Raman features. Powder XRD of the post laser-heated TcS_2 sample yields a crystalline pattern distinct from that of the $P\bar{1}$ phase (Fig. 3 bottom). A comprehensive XRD map confirms a homogeneous transformation of the sample into the new high pressure phase. Raman confirms a persistence of the new phase to ambient conditions as seen in the topmost spectrum of Fig. 3.

Crystal structure prediction[24] (CSP) calculations were employed to identify the new high pressure phase of TcS_2. Searching for structures with up to 4 formula units of TcS_2 at 20 GPa yields four candidate structures within $\sim$1 eV per formula unit of the lowest enthalpy structure. Three of the structures are monoclinic and the other is orthorhombic which in energetic order are $Cm > C2/m > Pnmn > P2_1/c$; their full structural information may be found in the ESI. The lowest enthalpy $P2_1/c$ phase is the arsenopyrite structure, and the orthorhombic $Pnmn$ structure is the marcasite structure. These extended 3-D structures are known phases for the 3d TMDCs, particularly MnS_2 and FeS_2, but are not commonly seen for the 4d and 5d TMDCs.[1,12] On the other hand, the monoclinic structures are both layered materials, more akin to the high pressure phases of the Re TMDCs which would be anticipated due to periodicity within group 7 and the assumption of analogous behavior between Tc and Re.[13,15,16] Another key difference between the two sets of predicted structures is that the extended arsenopyrite and marcasite structures both exhibit persulfide anions ($R_{S\text{–}S}$ $\sim$2.2 Å) indicative of a Tc^{2+} oxidation state while the layered structures retain atomic anions.

The candidate CSP structures were tested against the new XRD pattern, with the lowest enthalpy arsenopyrite phase providing the best match. Rietveld refinement with the $P2_1/c$ structural model at 28 GPa places a Tc and 2 symmetry inequivalent S atoms on 4e Wyckoff sites. The refined lattice has $a = 5.54772$ Å, $b = 5.57445$ Å, and $c = 5.60955$ Å ($V = 160.762$ Å^3), in good agreement with the DFT optimized 30 GPa $P2_1/c$ lattice ($a = 5.55$ Å, $b = 5.57$ Å, $c = 5.61$ Å). Further, Rietveld refinement confirms the the existence of S–S bonds (2.21 Å) and alternating short-long Tc–Tc nearest neighbor distances (2.692 and 3.543 Å), nearly identical to the 2.7 and 3.5 Å of the CSP structure. Agreement between the DFT phonon modes and Raman spectrum further confirms the new phase as $P2_1/c$. Full Rietveld analysis and Raman spectroscopy confirms no disproportionation or additional reactions occurred during laser heating.

Remarkably, the new high pressure phase of TcS_2 is the same structural type as MnS_2. This along with the pure element is another example of a Tc compound becoming more like Mn rather than Re when under pressure.[25] However unlike arsenopyrite MnS_2, the arsenopyrite phase of TcS_2 is completely recoverable to ambient conditions. The transformation into the arsenopyrite structure for TcS_2 is accompanied by a change in oxidation state, as the S–S bond of a persulfide anion is confirmed via an ELF (Fig. 2). The presence of persulfide-like interactions between the S atoms of different layers and the calculated ligand-to-metal charge transfer in compressed $P\bar{1}$ TcS_2 indicates that the phase transformation is driven by the formation of persulfide anions between the layers. The presence of the persulfide anions causes the electronic structure (Fig. 2c) of arsenopyrite TcS_2 to resemble a negative charge transfer insulator with a valence band composed primarily of Tc d states, and a conduction band with significant S p character. This new phase is insulative with predicted indirect band gaps of 0.785 eV at 20 GPa and 0.513 eV at 0 GPa; marking TcS_2 as another example of a pressure and temperature driven insulator-to-metal-to-insulator transition.

For MnS_2 there was a debate whether the high pressure phase was arsenopyrite or marcasite.[10] The major difference between these structures is the metal–metal nearest neighbor distances with the marcasite structure exhibiting evenly spaced metal atoms (3.04 Å for the CSP $Pnmn$ TcS_2). The alternating short-long metal–metal distances in the arsenopyrite structure are bonding interactions, making it akin to a Peierls-distorted version of the marcasite structure. It was found that a screened on-site

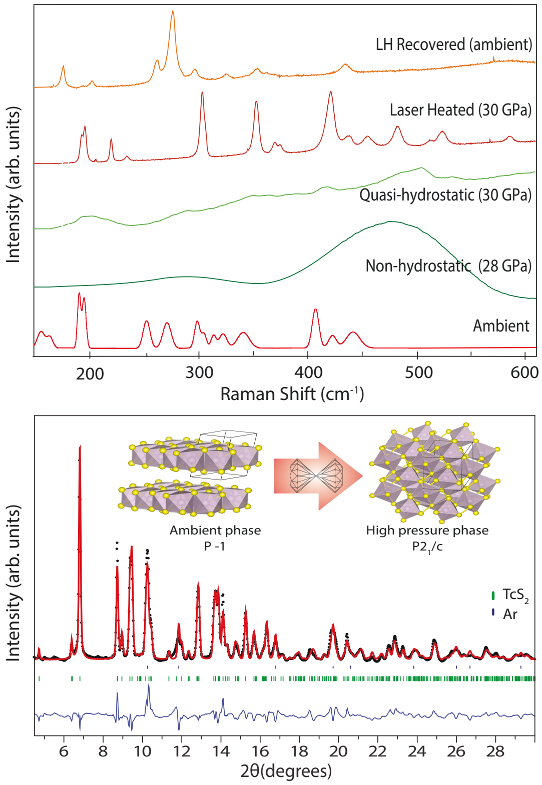

Fig. 3 Top: Raman shift of ambient starting material and its change under different compression environments, laser heating and recovered TcS_2, **Bottom:** XRD pattern of $P2_1/c$ TcS_2 at room temperature post laser heating. Data collected at $\lambda = 0.4246$ Å. Dark blue circles are the experimental data, the Rietveld refinement to $P2_1/c$ symmetry is shown in green, and the residual is shown in blue. All peaks were attributed to Ar or TcS_2; tick marks for each phase are shown below peaks. Crystal structures show the proposed structural change.

Coulomb interaction could induce magnetic ordering and equivalently spaced distances in arsenopyrite MnS_2.[11] Similar simulations on arsenopyrite TcS_2 showed a large correction is required to induce an antiferromagnetic state and equally spaced Tc–Tc nearest neighbors (more details are in the ESI). However, the enthalpic proximity of these two solutions and their close physical relation means it may be possible to access a TcS_2 marcasite phase through a different thermodynamic pathway.

In summary, $P\bar{1}$ TcS_2 undergoes a pressure-driven charge transfer insulator to metal transition which is completed by 46 GPa. This transition is driven by the interlayer separation decreasing to an extent that the S atoms on different layers can form S–S bonding-like interactions. Metallization is accompanied by pressure-induced amorphization with the emergence of a kinetically hindered high density phase. Laser heating at 30 GPa in an Ar PTM reveals a new high pressure phase, which has the arsenopyrite structure akin to MnS_2's high pressure phase. The arsenopyrite phase of TcS_2 exhibits persulfide molecular anions and Tc–Tc bonding. Adopting a high pressure phase similar to that of 3d Mn rather than the 5d Re, is a curious behavior for a 4d element, particularly Tc whose chemistry is often approximated with Re analogues. To date, the study of multiple compression pathways in the TMDCs is few but has led to interesting findings warranting further studies in other group 7 and 4d TMDCs.

This material is based upon work supported by the National Science Foundation Division of Materials Research under Grant No. 1904694. Portions of this work were performed at HPCAT (Sector 16), Advanced Photon Source (APS), Argonne National Laboratory. HPCAT operations are supported by DOE-NNSA Office of Experimental Sciences. The Advanced Photon Source is a U.S. Department of Energy (DOE) Office of Science User Facility operated for the DOE Office of Science by Argonne National Laboratory under Contract No. DE-AC02-06CH11357

Conflicts of interest

There are no conflicts to declare.

Notes and references

1 J. Wilson and A. Yoffe, *Adv. Phys.*, 1969, **18**, 193.
2 S. Tongay, H. Sahin, C. Ko, A. Luce, W. Fan, K. Liu, J. Zhou, Y. S. Huang, C. H. Ho, J. Yan, D. F. Ogletree, S. Aloni, J. Ji, S. Li, J. Li, F. M. Peeters and J. Wu, *Nat. Commun.*, 2014, **5**, 3252.
3 S. Manzeli, D. Ovchinnikov, D. Pasquier, O. V. Yazyev and A. Kis, *Nat. Rev. Mater.*, 2017, **2**, 17033.
4 Y. Zhang, Y. Yao, M. G. Sendeku, L. Yin, X. Zhan, F. Wang, Z. Wang and J. He, *Advanced Materials*, 2019, **31**, 1901694.
5 Q. Wang, Y. Lei, Y. Wang, Y. Liu, C. Song, J. Zeng, Y. Song, X. Duan, D. Wang and Y. Li, *Energy Environ. Sci.*, 2020, **13**, 1593.
6 Z.-H. Chi, X.-M. Zhao, H. Zhang, A. F. Goncharov, S. S. Lobanov, T. Kagayama, M. Sakata and X.-J. Chen, *Phys. Rev. Lett*, 2014, **113**, 036802.
7 H.-J. Lamfers, A. Meetsma, G. Wiegers and J. de Boer, *J. Alloy Compd.*, 1996, **241**, 34.
8 M. Tokuda, A. Yoshiasa, T. Mashimo, H. Arima, H. Hongu, T. Tobase, A. Nakatsuka and K. Sugiyama, *Z. Krist.-Cryst. Mater.*, 2019, **234**, 371.
9 B. Müller and H. Lutz, *Solid State Commun.*, 1991, **78**, 469.
10 D. Durkee, D. Smith, R. Torchio, S. Petitgirard, R. Briggs, I. Kantor, S. R. Evans, T. Chatterji, T. Irifune, S. Pascarelli, K. V. Lawler, A. Salamat and S. A. Kimber, *J. Solid State Chem.*, 2019, **269**, 540.
11 D. Durkee, N. Dasenbrock-Gammon, G. A. Smith, E. Snider, D. Smith, C. Childs, S. A. J. Kimber, K. V. Lawler, R. P. Dias and A. Salamat, *Phys. Rev. Lett.*, 2021, **127**, 016401.
12 S. A. J. Kimber, A. Salamat, S. R. Evans, H. O. Jeschke, K. Muthukumar, M. Tomić, F. Salvat-Pujol, R. Valentí, M. V. Kaisheva, I. Zizak and T. Chatterji, *Proc. Nat. Acad. Sci. U.S.A.*, 2014, **111**, 5106.
13 D. Hou, Y. Ma, J. Du, J. Yan, C. Ji and H. Zhu, *J. Phys. Chem Solids*, 2010, **71**, 1571.
14 Y.-C. Kao, T. Huang, D.-Y. Lin, Y.-S. Huang, K.-K. Tiong, H.-Y. Lee, J.-M. Lin, H.-S. Sheu and C.-M. Lin, *J. Chem. Phys.*, 2012, **137**, 024509.
15 P. Naumov, M. ElGhazali, H. Mirhosseini, V. Süß, E. Morosan, C. Felser and S. Medvedev, *J. Phys: Condens. Mat.*, 2017, **30**, 035401.
16 D. Zhou, Y. Zhou, C. Pu, X. Chen, P. Lu, X. Wang, C. An, Y. Zhou, F. Miao, C.-H. Ho *et al.*, *npj Quant Mater*, 2017, **2**, 19.
17 P. Wang, Y. Wang, J. Qu, Q. Zhu, W. Yang, J. Zhu, L. Wang, W. Zhang, D. He and Y. Zhao, *Phys. Rev. B*, 2018, **97**, 235202.
18 J. Zhang, E. Sun, X. Feng, H. Liu, S. A. T. Redfern, V. Kanchana, G. Liu and H. Wang, *Phys. Chem. Chem. Phys.*, 2018, **20**, 29472.
19 J. Wildervanck and F. Jellinek, *J. Less Common Metals*, 1971, **24**, 73–81.
20 Y. Joly, C. Cavallari, S. A. Guda and C. J. Sahle, *J. Chem. Theory Comput.*, 2017, **13**, 2172.
21 H. Peng, Z.-H. Yang, J. P. Perdew and J. Sun, *Phys. Rev. X*, 2016, **6**, 041005.
22 G. Henkelman, A. Arnaldsson and H. Jónsson, *Comp. Mater. Sci*, 2006, **36**, 354.
23 A. P. Nayak, S. Bhattacharyya, J. Zhu, J. Liu, X. Wu, T. Pandey, C. Jin, A. K. Singh, D. Akinwande and J.-F. Lin, *Nat. Commun.*, 2014, **5**, 3731.
24 A. O. Lyakhov, A. R. Oganov, H. T. Stokes and Q. Zhu, *Comp. Phys. Commun.*, 2013, **184**, 1172.
25 E. Siska, D. Smith, C. Childs, D. Koury, P. M. Forster, K. V. Lawler and A. Salamat, *Phys. Rev. Mater.*, 2021, **5**, 063603.